Available online at www.sciencedirect.com

ScienceDirect

Proceedings of the Combustion Institute 39 (2023) 521–529

Proceedings of the Combustion Institute

www.elsevier.com/locate/proci

How well do we know thermal-NO? An investigation of NO formation in flames over a wide temperature range

Marie Meulemans [a,*], Antoine Durocher [a], Philippe Versailles [a], Gilles Bourque [a,b], Jeffrey M. Bergthorson [a]

[a] *McGill University, 817 Sherbrooke St W,Montréal, QC H3A 0C3, Canada*
[b] *Siemens Energy Canada Limited, 9545 Chemin de la Côte-de-Liesse, Dorval, QC H9P 1A5, Canada*

Received 4 January 2022; accepted 24 July 2022
Available online 29 September 2022

Abstract

This study investigates the large variability and uncertainty in the thermal-initiation reaction rates found in the literature. An experimental study is conducted at atmospheric pressure in lean, premixed, laminar methane-air stagnation flames. Flame temperatures ranging from 1900K to 2500K are achieved by varying the argon concentration, in 21% and 40% oxygen mixtures balanced with nitrogen. The conditions are selected to promote the thermal route in the overall post-flame NO formation. One-dimensional velocity, temperature, and NO concentration profiles are measured with Particle Tracking Velocimetry (PTV), NO multi-line thermometry, and NO Laser-Induced Fluorescence (NO-LIF), respectively. While velocity and temperature measurements are accurately predicted by different thermochemical models, the simulated NO-LIF signal profiles show significant disagreement and large variability, relative to the measurements. Results show that, across all conditions, none of the studied mechanisms are able to capture accurately both the NO concentration, and formation rate in the post-flame region, suggesting that the fundamental chemistry remains inaccurate. The discrepancy in the predictions appears to be linked to the chosen parameters of the Arrhenius rate, specifically the pre-exponential factor, and the activation energy. Sensitivity and Reaction Pathway Analyses suggest that the differences in the Arrhenius parameters could originate from different consideration of the base radical chemistry, as well as different relative contributions of the four NO-formation routes. As a result, some models can predict similar NO concentrations but using significantly different underlying base and NO_x chemistry. This implies that the models could diverge significantly in conditions where other non-thermal routes are more important. This study demonstrates the need for spatially-resolved experimental data across a broad range of experimental conditions, promoting and considering a variety of routes, in order to optimize NO_x chemistry models with reduced uncertainty.
© 2022 The Combustion Institute. Published by Elsevier Inc. All rights reserved.

Keywords: CH_4 premixed flame; Nitric oxide; NO-laser induced fluorescence; NO pathways; Thermal route

* Corresponding author.
E-mail address: marie.meulemans@mail.mcgill.ca (M. Meulemans).
https://doi.org/10.1016/j.proci.2022.07.189
1540-7489 © 2022 The Combustion Institute. Published by Elsevier Inc. All rights reserved.

1. Introduction

Nitric oxide (NO) is highly regulated to limit its harmful impact on the environment and human health. The understanding of its formation is of interest to meet these regulations in practical systems. Many studies have been performed using a variety of experimental configurations and conditions to promote specific NO formation pathways, or routes, namely the prompt-NO, the NNH, the N_2O, and the thermal routes [1–6].

The main pathway to NO formation in traditional combustion applications is generally the thermal route, which scales with temperature and residence time. It has been extensively studied, experimentally and numerically, via its limiting reaction:

$$N_2 + O \underset{k_r}{\overset{k_f}{\rightleftharpoons}} NO + N \qquad \text{(R1)}$$

Despite its importance and the large amount of experimental data available, wide uncertainty and variability remains in the rate of the reaction, as shown for the reverse direction of R1 in Fig. 1.

In the compilation work of Baulch *et al.* [7], a recommended reaction rate for both, the forward (k_{1f}) and reverse (k_{1r}), directions are provided independently. However, when the reverse rate is derived from the recommended forward rate (k_{1f}) and the equilibrium constant (K_c), its value and uncertainty do not overlap the recommended reverse rate (k_{1r}) at high temperatures, see Fig. 1. This also shows the scatter of more recently determined rates, which suggests that the understanding of thermal-NO route, and thus the post-flame NO chemistry, remains uncertain.

Abián *et al.* [3] proposed a thermal-initiation rate (k_{1f}) using flow reactor measurements performed at temperatures ranging from 1700K to 1800K. However, lacking data to accurately derive Arrhenius rate coefficients, they used literature data to extrapolate a rate covering temperatures from 250-3000K, a more practical range of conditions. Buczkó *et al.* [8] characterized the uncertainty of this rate and provided corrected values, by considering the interaction of the N_2O pathway on the thermal rate. Similarly targeting the thermal rate, Han *et al.* [9] performed NO measurements on a heat flux burner using a wide range of conditions, and observed the interaction of the prompt and the thermal routes. As demonstrated, these studies account for different interactions of the NO formation pathways and thus infer different thermal-initiation rates. Therefore, it is still unclear how all the routes interact together, particularly in the post-flame region.

The objective of this study addresses this ambiguity by measuring NO over extreme temperature conditions, to promote the thermal NO pathway. The focus of this study is the post-flame region where the thermal pathway is dominant and NO

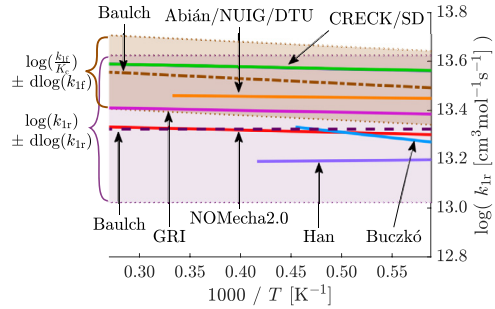

Fig. 1. Comparison of the reverse kinetic rate (k_{1r}) for the reaction $N_2 + O \rightleftharpoons NO + N$, of the mechanisms and references used in this study (–). k_{1r} as provided (- -) and calculated from k_{1f} and K_c (-·-) in Baulch *et al.* [7].

is most affected by the four routes. Additionally, the use of extreme conditions challenges six thermochemical models across a wide range of temperatures. These experiments are conducted in atmospheric, lean, premixed, methane-air stagnation flames, at flame temperatures ranging from 1900K to 2500K. Flame temperatures are reached by varying argon concentration, in 21% and 40% oxygen balanced in nitrogen. Spatially-resolved measurements are used, inline with current trends in the literature that increasingly recommend the use of time-resolved measurements to improve the predictions of thermochemical mechanisms, particularly those which involve complex formation pathways [10–12].

2. Experimental methods

An atmospheric jet-wall stagnation burner is used to conduct experiments in premixed flames. This provides accurate boundary conditions necessary for 1D simulations [13]. This setup, along with the diagnostic methods, have been detailed in [2,4,14–16].

The gas mixture is premixed before exiting the nozzle and impinging on a water-cooled stagnation plate located at a distance of ~9 mm. This provides a flat, lifted flame, minimally affected by the burner, as shown in Fig. 2. The flame is shielded from ambient air by a nitrogen coflow, improving stability and preventing chemical interference. Flame temperatures from 1900K to 2500K are used to promote the thermal pathway. These temperatures are reached by producing lean methane-air-argon flames at a constant equivalence ratio ($\phi = 0.9$) with two oxygen to nitrogen ratios: 21% and 40%. Argon dilution, up to 65% in the oxidizer stream, allows different flame temperatures to be obtained while maintaining the same stoichiometry. Mixture concentra-

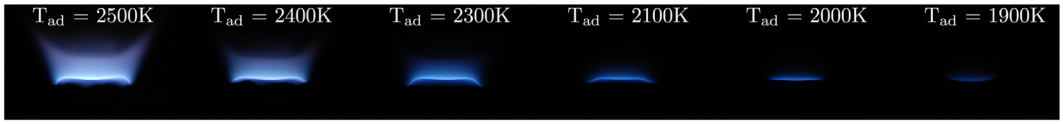

Fig. 2. Methane stagnation flames from $T_{ad} = 2500$K to 1900K obtained by argon dilution and enriched oxygen.

tions are defined as:

$$O_2\text{-to-}N_2 = \frac{N_{O_2}}{N_{O_2} + N_{N_2}}, \text{ and} \tag{1}$$

$$X_{Ar} = \frac{N_{Ar}}{N_{O_2} + N_{N_2} + N_{Ar}}, \tag{2}$$

where N_i is the molar concentration of species i.

The boundary conditions for the simulations are given in the Supplementary Material. The inlet velocity (u_{in}) and the strain rate (du_{in}/dz) are determined in the unburnt region of the axial velocity profile. The inlet temperature (T_{in}) and the stagnation plate temperature (T_{wall}) are measured during the experiments using thermocouples.

Axial velocity profiles are obtained by Particle Tracking Velocimetry (PTV) [15,17,18]. The laser beam illuminates the flow seeded with alumina (Al_2O_3 at 1μm avg. diameter) tracer particles, to track their instantaneous position. Camera exposures from 20 to 100ms and laser pulse frequencies from 4 to 10kHz are used (fixed for a given experiment). The acquisition of over 500 images allows the extraction of a 1D velocity profile of the tracer particle, u_p, along the central axis of the burner using a second-order central finite difference scheme, such that:

$$u_p(z_{p,i}, r_{p,i}) \approx \frac{z_{p,i+1} - z_{p,i-1}}{2} \cdot f \cdot C \tag{3}$$

at the particle location $z_{p,i}$ and $r_{p,i}$, and with f defined as the laser frequency in Hz, and C the camera calibration coefficient in mm/pixel. The direct comparison to simulated velocity profiles is possible through the modeling of the particle motion in the flow. The modeling accounts for drag due to thermophoretic force and particle inertia in high-gradient/high-curvature parts of the flow [19].

The NO concentration profiles are obtained using 2D Planar Laser Induced Fluorescence (PLIF) [4,5]. NO molecules are excited in the A–X (0,0) electronic system, using an Nd:YAG–pumped wavelength-tunable dye laser at a wavelength of ~226nm. The NO fluorescence is collected using an image intensified CCD camera at an exposure of 300ns and binned 4×8 (vertically and horizontally, respectively) to enhance signal-to-noise ratio. Signals of 2,000 images are captured at an online (S_{on}) and offline (S_{off}) wavelength of λ_{on}~226.03nm and λ_{off}~226.05nm, respectively, allowing the subtraction of interfering LIF and scattering signals. Signals are corrected for background noise (S_{bckg}) by capturing 200 images without laser irradiation and subtracting them from the samples to remove the effect of flame chemiluminescence, camera dark noise, and ambient luminosity. The resulting signal is normalized by the mean of the time-integrated laser pulse power of the online and offline signals, $E_{L,on}$ and $E_{L,off}$, respectively. Spatial fluctuations in the laser sheet are corrected by obtaining the LIF signal in an inert cold flow seeded with NO. For low laser irradiance, the signal F_{NO} is linearly proportional to NO number density as follows:

$$F_{NO} = \frac{(S_{on} - S_{bckg})}{E_{L,on}} - \frac{(S_{off} - S_{bckg})}{E_{L,off}}, \tag{4}$$

$$= f_{LIF} \cdot C_{opt} \cdot n^{\circ}_{NO}, \tag{5}$$

where f_{LIF} is the number of photons emitted per unit molecule of NO, per unit volume, and per laser energy, C_{opt} is the optical calibration coefficient accounting for optic transmitivity and camera sensitivity, and n°_{NO} is the number density of NO molecules. f_{LIF} is obtained using a two-level LIF model, allowing C_{opt} to be determined by calibration [2,5]. These are further explained in the Supplementary Material. Based on the *paradigm shift* presented by Connelly *et al.* [20], species concentration and temperature from the numerical solutions are used to derive numerical NO-LIF profiles, directly comparable to the measured NO-LIF profiles. This prevents the introduction of uncertainty through unit transformations of the experimental profiles, which require assumptions of temperature and quenching-species concentration (H_2O, O_2,...) that are not measured.

The NO-LIF profiles presented in this paper result from an average of several profiles obtained for each flame, from 2 to 7 measurements per condition, leading to a total of 48 flames used to determine C_{opt}. The experimental uncertainty associated with this measurement is calculated at z = 3.5 mm, and is reported on the NO-LIF profiles and on the subsequent figures. The large number of flames used for calibration leads to an uncertainty of less than 3% across all conditions, in the post-flame region. Details of the calculations are given in the Supplementary Material. The resulting NO-LIF profiles, while having a relatively high accuracy in the post-flame region, might still experience experimental uncertainty in the flame front due to the imaging system (image binning and point spread function), the chemiluminescence of the flame, as

well as the sharp change of density, NO concentration, and temperature of the flow.

Temperature profiles are measured using a multi-line NO-LIF thermometry approach [14,21]. The flames are seeded with a known concentration of NO (500ppm) to track the emitted fluorescence from the nozzle to the plate while varying the laser over 120 discrete wavelengths between $\lambda = 225.13$ nm and $\lambda = 225.19$ nm. The raw NO signal intensity and laser energy are measured similarly to the NO-LIF methodology. The unseeded and background signals are subtracted in order to maximize signal-to-noise ratio. For each wavelength, the NO signal is averaged over 50 laser pulses. An NO excitation spectrum is obtained for each pixel of the domain and is directly compared to LIF-Base [22] NO-excitation spectra, which vary with temperature, to determine the temperature field of the domain. A 1D temperature profile is extracted at the centerline of the nozzle and is directly compared to simulation results. This temperature measurement methodology leads to an uncertainty of ± 5% at 2000K [21]. While this methodology has proven successful in previous works, the excitation spectra are less sensitive for temperatures greater than 2300K, leading to increased uncertainty (see Fig. 3d).

3. Results and discussion

Three flames are stabilized at 21% oxygen-to-nitrogen ratio (O_2-to-N_2 = 21%, or 21%O_2) with different levels of argon dilution to reach adiabatic flame temperatures of 1900K, 2000K, and 2130K, and six flames at O_2-to-N_2 = 40% (40%O_2) to obtain adiabatic flame temperatures from 2000K to 2500K. An overlap at 2000K is used for both oxygen ratios to assess the role of the oxygen content on NO formation.

The predictive capabilities of several thermochemical models are evaluated by comparison to the measured profiles. In this paper, the following thermochemical models are evaluated: GRI–Mech3.0 (GRI) [23]; the San Diego 2016 mechanism (SD) with the 2018 NO_x chemistry [24]; the Chemical Reaction Engineering and Chemical Kinetics mechanism C1C3HT version 1412 (CRECK) [25]; the National University of Ireland, Galway mechanism NUIG-Mech1.1 (NUIG) [26] reduced to 206 species [27]; the Technical University of Denmark 2016 mechanism (DTU) [28]; and the Konnov 0.6 mechanism [29] with the NO_x chemistry of NOMecha2.0 [6] (KON). While the NOMecha2.0 submechanism has been optimized with the

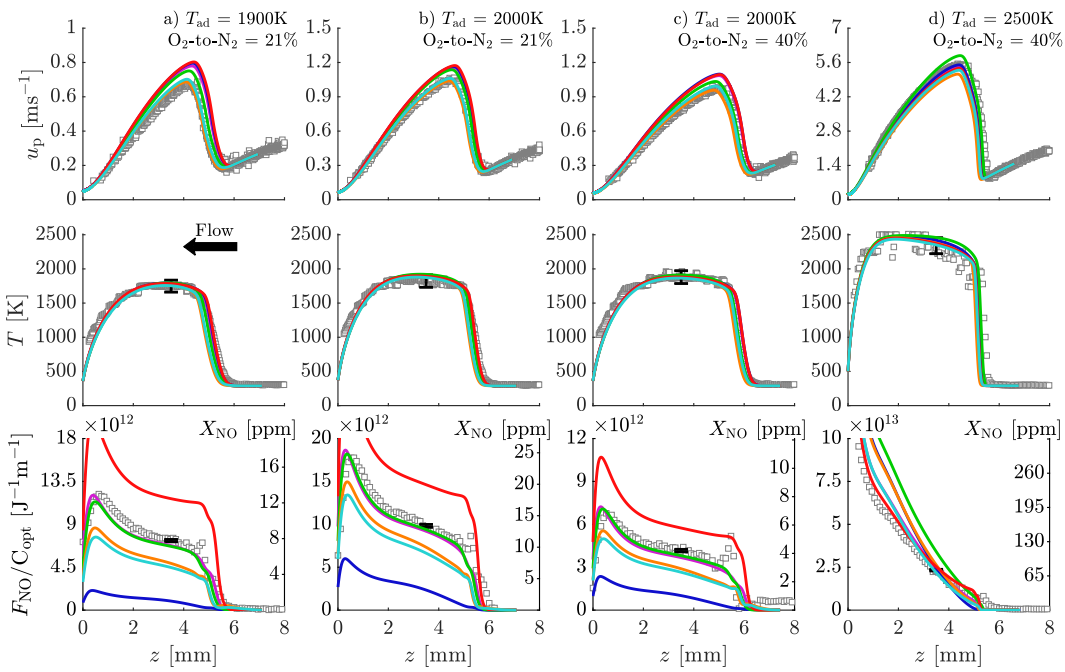

Fig. 3. Profiles of velocity (top), temperature (middle), and NO-LIF signal (bottom). Measured (□) and simulated (—) profiles are illustrated. Different thermochemical models are shown: GRI (—), SD (—), CRECK (—), NUIG (—), DTU (—) and KON (—). Note the different scales of the velocity and NO-LIF profiles. The vertical axes to the right of the NO-LIF signal profiles represent the estimate of NO concentration in ppm.

GDF–Kin3.0 base chemistry [30], the latter has shown large discrepancies in predicting velocity profiles of previous experiments [18]. Instead, NOMecha2.0 has been paired to Konnov 0.6 base chemistry, showing better agreement. Furthermore, both NUIG and DTU mechanisms have developed their NO_x chemistry based on the recent review paper by Glarborg *et al.* [31].

These simulations are performed using Cantera's *Impinging Jet* model [32], including multicomponent modeling of the transport coefficients, as well as radiative heat losses. The grids are refined to achieve criteria of 2, 0.05, and 0.05, for ratio, curve, and slope, respectively, with a 1μm minimum grid size, leading to solutions with ~350 gridpoints.

Velocity, temperature, and NO-LIF signals are presented in Fig. 3a–d, for the lowest (1900K), the two overlapping (2000K), and the highest (2500K) temperatures, respectively. The results of all nine flames are presented in the Supplementary Material. The flow exits the nozzle at z~9mm and impinges on the wall at $z = 0$ mm. Estimates of the NO concentration in ppm, valid for the post-flame region only, are extracted from the comparison to a reference mechanism, in this case GRI. These are presented on the right-hand vertical axis of the NO-LIF signal graphs. However, conclusions are drawn from F_{NO}/C_{opt} as this carries less uncertainty.

The general behavior of the measured velocity profiles is correctly described by the models. The particles decelerate gradually from the inlet to the flame front, reaching the reference flame speed $S_{u,ref}$, and then accelerate through the flame front due to thermal expansion of the flow. They decelerate again as the flow impinges on the stagnation plate. As expected from flame theory, $S_{u,ref}$ increases with T_{ad}. Additionally, there is little difference in velocity for the two oxygen contents at 2000K. Despite overall good agreement between the mechanisms in predicting the axial velocity of the particles, a slight difference in flame position and flame speed can be observed between the models and measurements. This discrepancy is amplified in the high-curvature and -velocity region downstream of the flame front, leading to an under-prediction of the velocity by DTU and NUIG and an over-estimation of the velocity by most other mechanisms considered.

For all cases, there is also good agreement between the measured and simulated temperature profiles. The temperature rises through the flame front to reach a maximum temperature of the order of the adiabatic temperature in the post-flame region. It then decreases through the wall thermal boundary layer to reach T_{wall}. Temperature predictions are within the uncertainty of the measurement technique.

The NO-LIF profiles have the characteristic sharp increase from flame-front NO (at z~6mm), and slow increase from the post-flame NO (from z~5mm to z~1.5mm). The signal increases near the plate (from z~1mm to $z = 0$ mm) from the change in NO density due to the thermal boundary layer. Additionally, at a spatial location, the NO signal increases with the increase in T_{ad}, as expected. As T_{ad} increases, the contribution of post-flame NO increases relative to the flame-front NO. Finally, at the overlap T_{ad}, a smaller NO concentration is produced at higher oxygen content as a larger dilution of Ar is needed. This leads to lower initial O- and N-atom availability, producing less NO.

In contrast to the temperature and velocity profiles, the measured NO-LIF profiles are only well described by a few thermochemical models, and a large variability of predictions can be observed over the entire range of temperatures. Discrepancies in both the flame-front and post-flame NO are present. The signal increase through the flame front is generally only properly captured by GRI and CRECK across all conditions, unlike KON which largely overpredicts it, and other mechanisms which underpredict it. These results support previous findings [1,2], where an important discrepancy was found in the prediction of CH concentration in these mechanisms for various fuels, leading to a misprediction of the prompt-NO produced through the flame front. In addition, the absence of the prompt initiation reaction in the SD model leads to a greater under-prediction of the NO produced in the entire profile. For low temperatures, the misprediction in the post-flame NO appears to be consistent with the discrepancies in the flame-front region. This shows that a correct description of the post-flame NO concentration requires an accurate description of the flame-front NO.

Furthermore, some mechanisms achieve good agreement with the measurements at specific points, despite having a strong disagreement throughout the rest of the profile. This can be seen on the NO-LIF profile for 2500K (Fig. 3d), where most mechanisms intersect the experimental profile at z~4mm. This demonstrates the necessity of including spatially- or time-resolved measurements to understand the origin of discrepancy in complex formation pathways.

To specifically target the post-flame region, comparisons between measurements and simulations of the NO-LIF signal are performed at $z =$ 3.5 mm. This location is far enough from the thermal boundary layer of the plate and allows enough time for the post-flame NO to develop. The analysis, at this location, of the absolute NO signal (F_{NO}/C_{opt}) is presented on Fig. 4a–c, and the analysis of the NO signal rate of change ($\mathrm{d}F_{NO}/(C_{opt} \cdot \mathrm{d}z)$) on Fig. 4d–f.

The ratio of the absolute NO signal is presented in Fig. 4b-c for 21%O_2 and 40%O_2, respectively. A perfect agreement between the models and measurements would be described by a ratio equal to unity. The shaded area represents

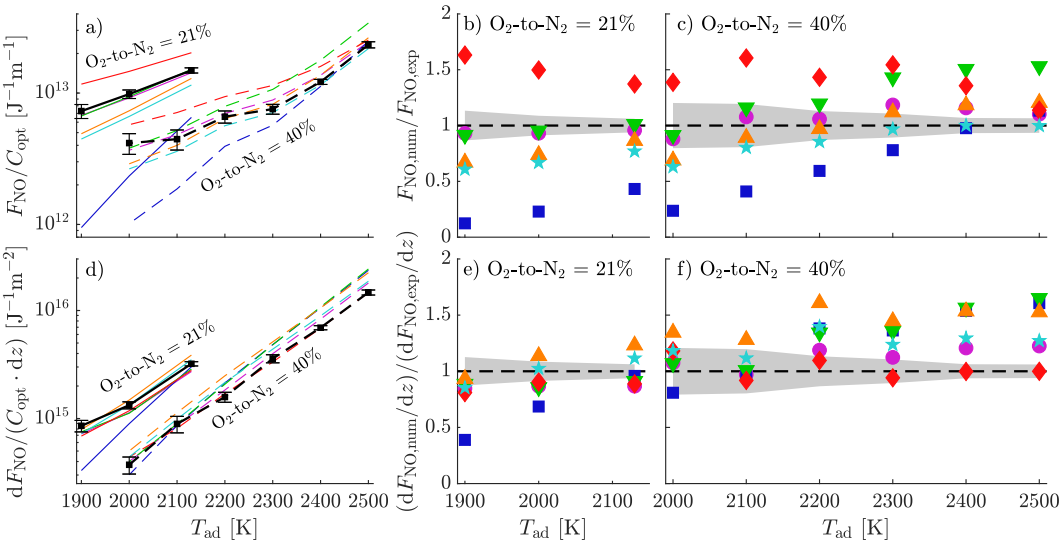

Fig. 4. Comparison of experimental (black lines and symbols) and numerical (colored lines and symbols), at $z = 3.5$ mm for: a) Absolute NO-LIF signal, b–c) Ratio of numerical to experimental absolute NO-LIF signals, d) NO-LIF signal slope, e–f) Ratio of numerical to experimental NO-LIF signal slopes. Different thermochemical models represented by the following colors and lines: GRI (●), SD (■), CRECK (▼), NUIG (▲), DTU (★) and KON (♦). Shaded areas represent the root-sum square of both the experimental and numerical uncertainties.

the root-sum square of both the experimental and the numerical uncertainties, the latter emanating from uncertainty in the estimated boundary conditions. A larger uncertainty (~20%) is present for low temperature measurements as they produce less NO, leading to smaller LIF signal-to-noise ratio. Conversely, there is lower uncertainty (~6%) at high temperature due to higher signal-to-noise ratio from increased NO production. These uncertainties make these experimental datasets valuable additions to model optimization.

The figures show that the difference between the measurements and simulations, for both oxygen contents, changes with temperature. The large variability of predictions is mostly present at low temperatures, and appears to stem mostly from the flame-front NO prediction, as observed in Fig. 3. This again indicates that the flame-front NO is not accurately captured, and its misprediction impacts mostly conditions where thermal NO is not dominant. Similar to previous observations, only CRECK and GRI capture the absolute NO signals at 3.5 mm, up to 2200 K.

To better understand the prediction of post-flame NO by the mechanisms, the rate of change of the signal $\left(dF_{NO}/(C_{opt} \cdot dz)\right)$, or slope of F_{NO}/C_{opt}, is calculated for the measured and simulated profiles. It is determined by a linear regression of the signals between 2 and 4.5mm. The values are presented in Fig. 4d and ratios of numerical to experimental values in Fig. 4e-f for 21%O_2 and 40%O_2, respectively. Overall, all mechanisms tend to be in reasonable agreement with the measured NO rate of formation at temperatures below 2200K. From 2200K, all mechanisms, except for KON, exhibit significant discrepancies. In contrast, KON reasonably predicts the post-flame NO rate of formation, across the entire range of temperatures, despite the significant overprediction of the flame-front NO.

Interestingly, it is at the highest temperature, where the mechanisms are most challenged, that the widest spread of predictions can be observed in between the different models. At this condition, despite the small experimental and numerical uncertainty, KON precisely predicts $dF_{NO}/(C_{opt} \cdot dz)$. In contrast, CRECK overpredicts the rate of formation by 65%. These results can directly be correlated with the Arrhenius rates illustrated in Fig. 1. KON (NOMecha2.0) possesses the best agreement with the slope measurements at 2500K and it uses a rate with the lowest pre-exponential factor (A), and is inline with the recommended k_{1r} from Baulch *et al.* [7]. Furthermore, GRI, DTU & NUIG, and CRECK & SD, in this order, possess an increasing pre-exponential factor, and Fig. 4f shows that their overprediction is also in the same order. This demonstrates that the error in prediction of $dF_{NO}/(C_{opt} \cdot dz)$ grows with A. Additionally, KON seems to accurately predict the correlation of the slope with temperature, indicating an accurate definition of the activation energy (E_a). These nuances in the reaction rates of each model could cause the differences in predictions in Fig. 4.

The sources of the differences in the models is explored in Fig. 5 with a Sensitivity Analysis performed on the NO rate of formation at $z = 3.5$

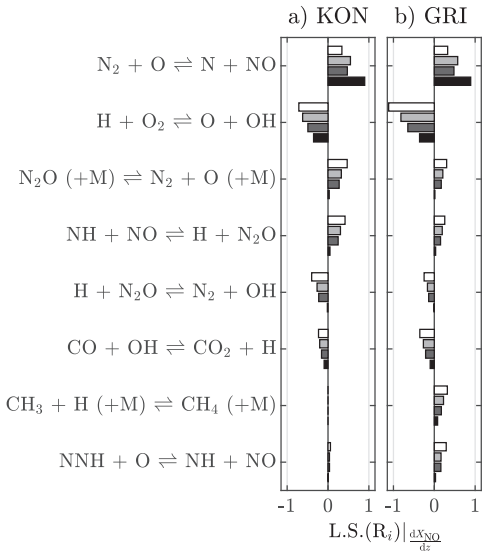

Fig. 5. Sensitivity Analysis performed on dX_{NO}/dz, for the KON (a) and GRI (b) mechanisms, using $dk = 1\%$ on each reaction. Bars represent the four flames of Fig. 3, 1900K-21%O_2 (white), 2000K-21%O_2 (light grey), 2000K-40%O_2 (dark grey), 2500K-40%O_2 (black).

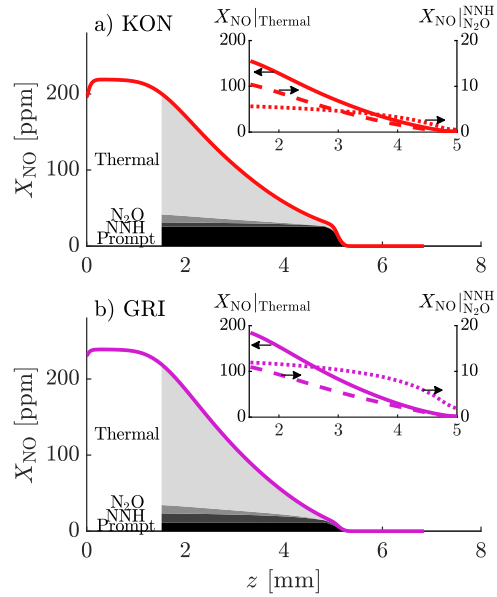

Fig. 6. Reaction Pathway Analysis performed on the flame at 2500K, using the KON (a) and GRI (b) mechanisms. Estimates of the NO produced by each route in the post-flame region are illustrated in each subfigure: thermal (—), N_2O (– –), and NNH (···).

mm, on the reactions of the KON and GRI mechanisms. This analysis demonstrates that the slope is most sensitive to the thermal-initiation reaction (N_2 + O), across the studied temperatures. As expected, the influence of this reaction on the slope increases with temperature. In contrast, the reaction H + O_2, driving O-atom production, is inversely correlated with the slope, and its impact reduces with temperature. This illustrates the importance of an accurate base radical chemistry to precisely predict NO production as it controls the radical pool size, for the entire range of temperatures, and especially at low temperatures. The set of reactions involved in defining the slope of NO though the N_2O pathway, has a reduced impact with increasing temperature. However, its influence at low temperatures is of similar order to the thermal. This shows that the N_2O pathway is particularly important in defining the thermal rate at lower temperatures. A similar observation can be made with the NNH reaction that is of more significant importance for GRI compared to KON.

These results demonstrate the importance of accurately predicting the N_2O and NNH pathways, and the base radical chemistry, as they have a significant influence on the post-flame NO. Therefore, if models would recommend an accurate thermal-initiation rate, they would require accurate modeling of each of the NO-producing pathways and the base radical chemistry. This could aid in resolving the variability of the thermal-initiation rate, shown in Fig. 1, via the A and E_a parameters.

As the Sensitivity Analysis showed the importance of the N_2O pathway, a Reaction Pathway Analysis (RPA) is performed to determine the contribution of all four routes to the overall NO production. This is conducted on the 2500K flame, following the methodology established by Grcar *et al.* [33] and Versailles [17]. The analysis is performed using the KON and GRI mechanisms, which offer the best agreement at 2500K regarding the absolute NO concentration and formation rate in the post-flame region. Fig. 6 presents the relative share of the four routes (prompt, NNH, N_2O, and thermal) to the overall NO formation. Individual absolute contributions to NO formation of the thermal, N_2O, and NNH routes are also provided in the subfigures. As expected from the analysis of the thermal-initiation rate, KON predicts lower absolute contribution of the thermal-NO compared to GRI. Furthermore, the prompt overprediction of KON shown in Fig. 3, is also observed in the RPA.

While the two mechanisms predict a similar total NO production, they display significant differences in the relative contributions of the four pathways, for both the flame-front NO and the post-flame NO production. As a result, despite similar absolute NO predictions, the thermal-initiation rate that would be inferred by the models, could stem from differences in the importance placed upon, not only the N_2O pathway, but also the NNH and prompt pathways. This suggests that the fun-

damental chemistry governing NO production remains not well understood.

4. Conclusion

In this study, a stagnation flame burner under controlled boundary conditions is used to measure the velocity, temperature, and NO concentration profiles, using Particle Tracking Velocimetry (PTV), NO multi-line thermometry, and NO laser-induced fluorescence (NO-LIF), respectively. The measurements are performed on nine flames using two levels of oxygen concentration, 21% and 40%O_2, as well as argon dilution to reach adiabatic flame temperatures ranging from 1900K to 2500K. 1D simulated profiles are compared to the results using six thermochemical models.

Measurements are performed in conditions to promote the thermal-NO pathway. Large variability in predictions of the NO-LIF profiles show that none of the considered mechanisms are able to predict accurately the produced NO concentration and the NO rate of formation in the post-flame region, revealing that the fundamental chemistry of NO formation remains inaccurate. Analysis of the discrepancy between measurements and simulations demonstrate that the prediction of post-flame NO by the models, is directly related to their definition of the thermal-initiation rate, specifically the pre-exponential factor A, and the activation energy E_a.

Sensitivity and Reaction Pathway Analyses indicate that the discrepancy in the definition of the thermal-initiation reaction could result from different consideration of the base radical chemistry, and the contribution of other NO formation routes. This paper shows that it is possible to predict NO concentrations and NO formation rates that are in reasonable agreement with experiments, but with different underlying chemistry. This suggests that the model predictions would significantly diverge under conditions where non-thermal routes become increasingly important.

To address this, future efforts in optimizing NO_x chemistry should employ measured NO profiles across a broad range of experimental conditions, which promote a variety of NO formation pathways. This would allow the development of models with reduced uncertainty and increased predictive capability to further improve the emissions of state-of-the-art combustion technologies.

Supplementary Material

Supplementary Material presents: the experimentally-measured boundary conditions, the calibration of optical constant C_{opt}, the uncertainty calculation, and the full set of measured profile figures. The full set of experimental data are included in an Excel file.

Declaration of Competing Interest

The authors declare that they have no known competing financial interests or personal relationships that could have appeared to influence the work reported in this paper.

Acknowledgments

The authors would like to acknowledge the contribution of Siemens Energy Canada, the National Research Council Canada (NRC), and the Réseau Québécois sur lÉnergie Intelligente (RQEI).

Supplementary material

Supplementary material associated with this article can be found, in the online version, at doi:10.1016/j.proci.2022.07.189.

References

[1] P. Versailles, G.M.G. Watson, A.C.A. Lipardi, J.M. Bergthorson, Quantitative CH measurements in atmospheric-pressure, premixed flames of C_1-C_4 alkanes, Combust. Flame 165 (2016) 109–124.
[2] G.M.G. Watson, P. Versailles, J.M. Bergthorson, NO formation in premixed flames of C_1-C_3 alkanes and alcohols, Combust. Flame 169 (2016) 242–260.
[3] M. Abián, M.U. Alzueta, P. Glarborg, Formation of NO from N_2/O_2 mixtures in a flow reactor: Toward an accurate prediction of thermal NO, Int. J. Chem. Kinet. 47 (8) (2015) 518–532.
[4] P. Versailles, A. Durocher, G. Bourque, J.M. Bergthorson, Nitric oxide formation in lean, methane-air stagnation flames at supra-atmospheric pressures, Proc. Combust. Inst. 37 (1) (2019) 711–718.
[5] A. Durocher, M. Meulemans, P. Versailles, G. Bourque, J.M. Bergthorson, Back to basics - NO concentration measurements in atmospheric lean-to-rich, low-temperature, premixed hydrogen-air flames diluted with argon, Proc. Combust. Inst. 38 (2021) 2093–2100.
[6] N. Lamoureux, H.E. Merhubi, L. Pillier, S. de Persis, P. Desgroux, Modeling of NO formation in low pressure premixed flames, Combust. Flame 163 (2016) 557–575.
[7] D.L. Baulch, C.T. Bowman, C.J. Cobos, R.A. Cox, T. Just, J.A. Kerr, M.J. Pilling, D. Stocker, J. Troe, W. Tsang, R.W. Walker, J. Warnatz, Evaluated kinetic data for combustion modeling: Supplement II, J. Phys. Chem. Ref. Data 34 (3) (2005) 757–1397.
[8] N.A. Buczkó, T. Varga, I.G. Zsély, T. Turányi, Formation of NO in high-temperature $N_2/O_2/H_2O$ mixtures: re-evaluation of rate coefficients, Energy Fuels 32 (10) (2018) 10114–10120.
[9] X. Han, L.L. Marco, C. Brackmann, Z. Wang, Y. He, A.A. Konnov, Experimental and kinetic modeling study of NO formation in premixed $CH_4+O_2+N_2$ flames, Combust. Flame 223 (2021) 349–360.
[10] O. Mathieu, C.R. Mulvihill, E.L. Petersen, Assessment of modern detailed kinetics mechanisms to predict CO formation from methane combustion using

shock-tube laser-absorption measurements, Fuel 236 (2019) 1164–1180.

[11] Y. Zhang, O. Mathieu, E.L. Petersen, G. Bourque, H.J. Curran, Assessing the predictions of a NO_x kinetic mechanism on recent hydrogen and syngas experimental data, Combust. Flame 182 (2017) 122–141.

[12] R.K. Hanson, D.F. Davidson, Recent advances in laser absorption and shock tube methods for studies of combustion chemistry, Prog. Energy Combust. Sci. 44 (2014) 103–114.

[13] R.J. Kee, J.A. Miller, G.H. Evans, G. Dixon-Lewis, A computational model of the structure and extinction of strained, opposed flow, premixed methane-air flames, Symp. Combust. (1988) 1479–1494.

[14] P. Versailles, A. Durocher, G. Bourque, J.M. Bergthorson, Effect of high pressures on the formation of nitric oxide in lean, premixed flames, J. Eng. Gas Turbines Power 143 (2021) 051029.

[15] A. Durocher, M. Meulemans, G. Bourque, J.M. Bergthorson, Measurements of the laminar flame speed of premixed, hydrogen-air-argon stagnation flames, Appl. Energy Combust. Sci. 7 (2021) 100028.

[16] A.C.A. Lipardi, P. Versailles, G.M.G. Watson, G. Bourque, J.M. Bergthorson, Experimental and numerical study on NO_x formation in CH_4-air mixtures diluted with exhaust gas components, Combust. Flame 179 (2017) 325–337.

[17] P. Versailles, CH formation in premixed flames of C_1-C_4 alkanes: assessment of current chemical modelling capability against experiments, McGill University, 2017.

[18] P. Versailles, A. Durocher, G. Bourque, J.M. Bergthorson, Measurements of the reactivity of premixed, stagnation, methane-air flames at gas turbine relevant pressures, J. Eng. Gas Turbines Power 141 (2019) 011027.

[19] J.M. Bergthorson, P.E. Dimotakis, Particle velocimetry in high-gradient/high-curvature flows, Exp. Fluids 41 (2006) 255–263.

[20] B.C. Connelly, B.A. Bennett, M.D. Smooke, M.B. Long, A paradigm shift in the interaction of experiments and computations in combustion research, Proc. Combust. Inst. 32 I (1) (2009) 879–886.

[21] W.G. Bessler, C. Schulz, Quantitative multi-line NO-LIF temperature imaging, Appl. Phys. B Lasers Opt. 78 (2004) 519–533.

[22] J. Luque, D.R. Crosley, LIFBASE version 2.1.1, database and spectral simulation for diatomic molecules (v1.6), 1999

[23] G.P. Smith, D.M. Golden, M. Frenklach, N.W. Moriarty, B. Eiteneer, M. Goldenberg, T. Bowman, R.K. Hanson, S. Song, W.C. Gardiner, V.V. Lissianski, Z. Qin, GRI-Mech 3.0 (1999).

[24] University of California at San Diego, Chemical-Kinetic Mechanisms for Combusiton Applications (2016).

[25] E. Ranzi, A. Frassoldati, R. Grana, A. Cuoci, T. Faravelli, A.P. Kelley, C.K. Law, Hierarchical and comparative kinetic modeling of laminar flame speeds of hydrocarbon and oxygenated fuels, Prog. Energy Combust. Sci. 38 (2012) 468–501.

[26] Y. Wu, S. Panigrahy, A.B. Sahu, C. Bariki, J. Beeckmann, J. Liang, A.A. Mohamed, S. Dong, C. Tang, H. Pitsch, Z. Huang, H.J. Curran, Understanding the antagonistic effect of methanol as a component in surrogate fuel models: a case study of methanol/*n*-heptane mixtures, Combust. Flame 226 (2021) 229–242.

[27] M. Kelly, S. Dooley, G. Bourque, Toward machine learned highly reduced kinetic models for methane/air combustion, in: Proceedings of the ASME Turbo Expo, 2021. V03AT04A005

[28] H. Hashemi, J.M. Christensen, S. Gersen, H. Levinsky, S.J. Klippenstein, P. Glarborg, High-pressure oxidation of methane, Combust. Flame 172 (2016) 349–364.

[29] A.A. Konnov, Implementation of the NCN pathway of prompt-NO formation in the detailed reaction mechanism, Combust. Flame 156 (2009) 2093–2105.

[30] A. El Bakali, L. Pillier, P. Desgroux, B. Lefort, L. Gasnot, J.F. Pauwels, I. Da Costa, NO prediction in natural gas flames using GDF-Kin3.0 mechanism NCN and HCN contribution to prompt-NO formation, Fuel 85 (7-8) (2006) 896–909.

[31] P. Glarborg, J.A. Miller, B. Ruscic, S.J. Klippenstein, Modeling nitrogen chemistry in combustion, Prog. Energy Combust. Sci. 67 (2018) 31–68.

[32] D.G. Goodwin, R.L. Speth, H.K. Moffat, B.W. Weber, Cantera: An object-oriented software toolkit for chemical kinetics, thermodynamics, and transport processes, Version 2.5 (2021).

[33] J.F. Grcar, M.S. Day, J.B. Bell, A taxonomy of integral reaction path analysis, Combust. Theory Model. 10 (4) (2006) 559–579.